

# Loss mechanisms of microwave frequency acoustic waves in thin film lithium niobate

Qixuan Lin,<sup>1</sup> Yue Yu,<sup>1</sup> Alejandra Guedea-Marrón,<sup>2</sup> Catalina Scolnic,<sup>2</sup> Haoqin Deng,<sup>1</sup> Shucheng Fang,<sup>1</sup> Yibing Zhou,<sup>1</sup> Bingzhao Li,<sup>1</sup> Juan Carlos Idrobo,<sup>2,3</sup> and Mo Li<sup>1,4</sup>

<sup>1)</sup>*Department of Electrical and Computer Engineering, University of Washington, Seattle, WA 98115, USA*

<sup>2)</sup>*Materials Sciences and Engineering Department, University of Washington, Seattle, WA 98115, USA.*

<sup>3)</sup>*Physical and Computational Sciences Directorate, Pacific Northwest National Laboratory, Richland, WA 99354, USA.*

<sup>4)</sup>*Department of Physics, University of Washington, Seattle, WA 98115, USA*

(\*Electronic mail: moli96@uw.edu)

(Dated: 4 February 2026)

Thin-film lithium niobate (TFLN) has emerged as a versatile platform for phononic and photonic devices with applications ranging from classical signal processing to quantum technologies. However, acoustic loss fundamentally limits the performance of acoustic devices on TFLN platforms, yet its physical origin remains insufficiently understood. Here, we systematically investigate acoustic propagation loss in various TFLN platforms, including lithium niobate on insulator (LNOI), lithium niobate on sapphire (LNOS), suspended LN thin films, and bulk LN at gigahertz frequencies over temperatures ranging from 4 K to above room temperature. Using a delay-line method, we extract frequency- and temperature-dependent losses for Rayleigh, shear-horizontal, and Lamb modes. We observe an anomalous non-monotonic temperature dependence in LNOI that closely resembles acoustic loss in amorphous materials, indicating a dominant loss channel associated with the buried oxide layer at low temperatures. At elevated temperatures, the loss converges to the Akhiezer damping governed by phonon-phonon interactions. High-resolution electron microscopy further reveals nanoscale interfacial crystal impurities that may contribute to the increased acoustic loss in TFLN platforms relative to bulk LN. These results elucidate the acoustic loss mechanisms in TFLN and provide guidelines for designing low-loss acoustic devices.

Surface acoustic waves (SAWs), including Rayleigh, Lamb, Love, and shear-horizontal (SH) waves, have become increasingly important for a wide range of modern micro- and nano-mechanical technologies. Owing to their velocities being approximately five orders of magnitude lower than those of electromagnetic waves, acoustic waves can be excited at microwave frequencies with micrometer-scale wavelengths. This unique property enables compact SAW microwave filters<sup>1,2</sup>, acousto-optic devices<sup>3,4</sup>, and quantum devices<sup>5–9</sup>. In addition, SAWs generate oscillating strain, displacement, and, in piezoelectric materials, accompanying electric fields, traveling in a continuous medium. These fields can strongly interact with particles<sup>10</sup>, solid-state quantum systems, such as excitons, electron spins, and defect-related states<sup>11–16</sup>. SAW also couples with light, especially guided modes in integrated photonics, thereby enabling optomechanical and acousto-optic devices for advanced optical sensing<sup>3,17</sup>, communication<sup>4,18–20</sup>, and quantum transduction<sup>5,21,22</sup>.

Among many piezoelectric materials that are employed for SAW devices, lithium niobate (LN) stands out for its strong piezoelectricity and excellent mechanical and optical properties<sup>1,8,23,24</sup>. SAW with low propagation loss can be efficiently generated on LN, and high-performance SAW filters have been demonstrated on bulk LN. Recently, thin-film lithium niobate (TFLN) platforms, including lithium niobate on insulator (LNOI), lithium niobate on sapphire (LNOS), and suspended LN thin film, have emerged for many acoustic and optical applications. They support co-guided optical

and acoustic modes with enhanced mode confinements and interaction strength. They enable efficient acousto-optic<sup>3,4</sup> and piezo-optomechanical devices<sup>21,25</sup>. In addition, non-suspended TFLN substrates offer improved mechanical robustness and power-handling capability, making them particularly attractive for integrated SAW-photonic platforms.

However, TFLN platforms, especially non-suspended ones, suffer from a significantly higher acoustic loss than that of bulk LN<sup>19,26,27</sup>. The resulting loss of acoustic energy degrades device performance, for example, reducing acousto-optic interaction efficiency<sup>19</sup>. Acoustic loss mechanisms in bulk lithium niobate (LN) have been extensively studied. For instance, Slobodnik et al.<sup>23</sup> reported that, for Rayleigh-mode surface acoustic waves in bulk LN at 1 GHz, the total propagation loss consists of a temperature-dependent propagation loss of 0.23 dB/mm at room temperature, an air-loading loss of 0.016 dB/mm, and a temperature-independent intrinsic propagation loss of 0.016 dB/mm. In contrast, a comprehensive study of the underlying acoustic loss mechanisms in TFLN platforms has not yet been reported and is therefore imperative.

Acoustic loss in solids arises from various mechanisms, such as phonon-phonon interaction, air loading, and scattering by material impurities<sup>23,28</sup>. At low temperatures, acoustic loss due to coupling to two-level systems (TLS) becomes significant<sup>16,27,29,30</sup>. Distinguishing among these loss mechanisms is essential for the design and optimization of the mechanical performance of acoustic devices on TFLN substrates.

In this work, we systematically analyze acoustic loss mech-

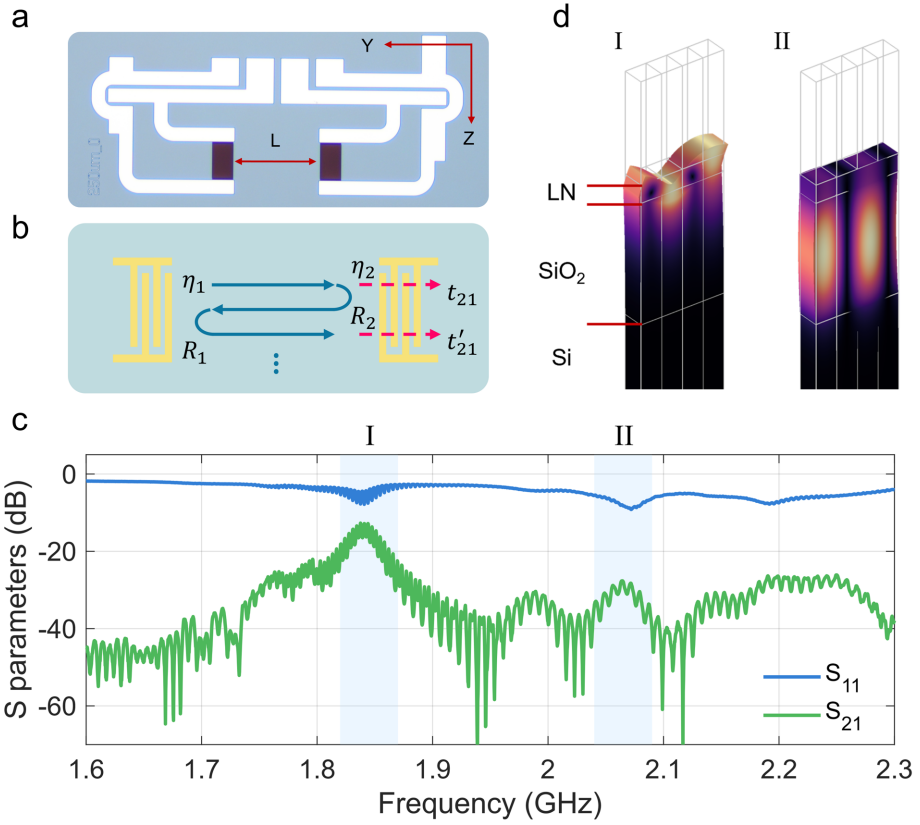


**FIG. 1. Device design and measurement principle.** (a). An optical microscope image of an IDT pair fabricated on x-cut LNOI substrate. Two slightly chirped IDTs are fabricated along the LN  $y$ -axis with a delay length  $L$ . (b) Schematic illustration of acoustic propagation loss measurement scheme using a delay line. (c). Representative S-parameter measurement results of the device. Region I and II correspond to the excitation of Rayleigh and shear-horizontal acoustic modes, respectively. (d). Finite-element-method (FEM) simulations showing the displacement field distributions of the two acoustic modes.

anisms of TFLN by measuring propagation loss in four different platforms: (A) x-cut LNOI consisting of a 300-nm-thick LN layer on a 2- $\mu\text{m}$  buried oxide on a silicon handle wafer, a structure which is widely used for integrated photonics; (B) x-cut LNOS consisting of a 400-nm-thick LN layer on sapphire handle wafer; (C) bulk 128° YX-cut LN; and (D) a free-standing LN thin film realized by undercutting the LNOI structure in platform A. By characterizing both the frequency and temperature dependence of the acoustic propagation loss across these material platforms, we gain insight into the acoustic loss mechanisms in TFLN devices.

The acoustic propagation loss is measured using a delay-line method. A pair of interdigital transducers (IDTs) separated by a delay length  $L$  is fabricated to excite and receive acoustic waves, as shown in Fig. 1(a). On samples A, B, and D, the acoustic waves propagate along the  $y$ -axis of the LN crystal, whereas on sample C, they propagate along the  $x$ -axis. A vector network analyzer (VNA) is used to apply drive signals of microwave frequencies to the first IDTs and measure the signals from the second IDTs to determine the device's S-parameters. Frequency-domain measurement results can be transformed to the time domain for further analysis.

Fig. 1(b) illustrates the delay line measurement principle

for acoustic propagation loss. An acoustic pulse generated by the first IDT travels in the material and arrives at the second IDT after a transit time  $\tau = L/v_g$ , where  $L$  is the distance between the two IDTs and  $v_g$  is the acoustic group velocity. At the receiving IDT, part of the acoustic energy is detected while part of it is reflected, which travels back and forth to form a sequence of echoes with sequential delay times of  $2\tau$ . The transmission coefficient of the electrical signal through the first-arriving acoustic wave packet can be written as

$$t_{21} = \eta_1 \eta_2 e^{-\alpha L} \quad (1)$$

and the transmission coefficient of the second arriving wave packet, after one reflection at each IDT, is

$$t'_{21} = \eta_1 \eta_2 r_1 r_2 e^{-3\alpha L} \quad (2)$$

where  $\eta_1$  ( $\eta_2$ ) denotes the acoustic wave excitation (receiving) efficiencies by the excitation (receiving) IDT, and  $r_1$  and  $r_2$  are reflectivities of acoustic waves at the two IDTs, respectively. Therefore, the ratio of the amplitudes of two wave packets is:

$$\gamma(L) = \frac{t_{21}}{t'_{21}} = e^{2\alpha L} / (r_1 r_2) \quad (3)$$

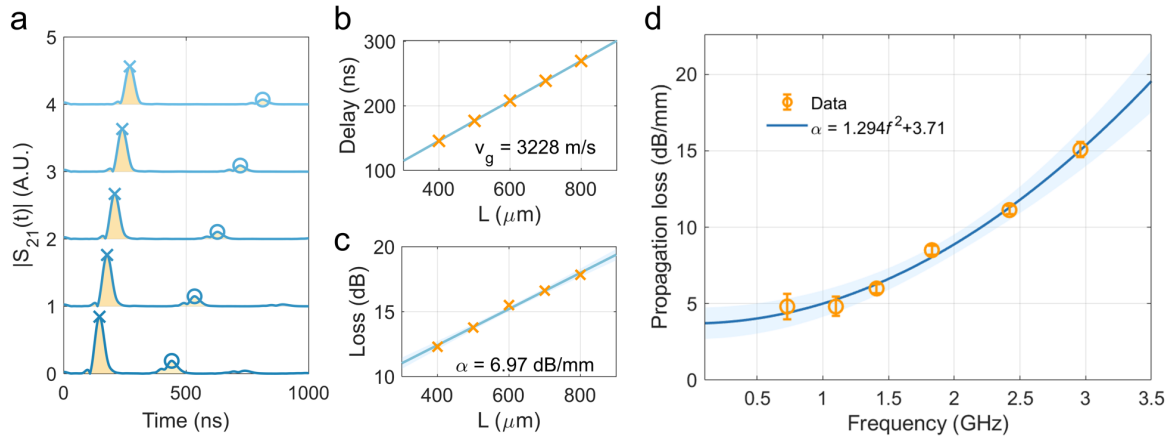


**FIG. 2. Acoustic loss measurement using a delay-line method.** (a). Time-domain signals obtained by taking the inverse Fourier transform of the  $S_{12}$  response within the 1.82–1.87 GHz frequency range. Each trace corresponds to an IDT pair with a different delay length  $L$ , varying from 400  $\mu\text{m}$  (bottom) to 800  $\mu\text{m}$  (top), with vertical offsets applied for clarity. The shaded wave packets indicate acoustic pulses arriving at the receiving IDT via direct transmission or multiple round-trip reflections. Cross and circle markers denote the peak amplitudes of the first and the second arrival wave packets, respectively. Measurements are performed at room temperature. (b). Acoustic group velocity extracted from a linear fit of the delay time of the first wave packet as a function of the corresponding delay length. (c). A 6.97 dB/mm propagation loss extracted from a linear fit of the measured amplitude ratio between the first and the second wave packets at different delay lengths  $L$ . (d). Frequency dependence of acoustic propagation loss, fitted with a quadratic function of frequency. The shaded regions in this figure and the following indicate the 95% confidence interval.

, where  $\eta_1$  ( $\eta_2$ ), which will need independent calibration, are canceled out. We fabricate a set of devices with identical IDT designs and fabrication processes, but with varying delay lengths  $L$ . Assuming that the acoustic reflectivity  $r_1(r_2)$  remain constant across these devices, the acoustic propagation loss  $\alpha$  is extracted by fitting  $\gamma(L)$  as a function of  $L$ .

Fig. 1(c) shows the measured S-parameters, reflection coefficient  $S_{11}$  and transmission coefficient  $S_{21}$ , of a representative device fabricated on sample A. Each IDT consists of 25 pairs of electrode fingers with a slightly chirped pitch ranging from 1.5  $\mu\text{m}$  to 1.65  $\mu\text{m}$  and a constant duty cycle of 50%. The two shaded regions, I and II, correspond to the excitation of the fundamental Rayleigh mode and shear-horizontal (SH) mode, respectively. The corresponding displacement field distributions for the two modes, simulated using the finite-element method, are shown in Fig. 1(d).

We first focus on the Rayleigh mode in the 1.82–1.87 GHz frequency range. All measurements are conducted at room temperature unless otherwise noted. By applying a window over the selected frequency band and performing an inverse Fourier transform of the measured  $S_{21}(f)$ , we obtain the time-domain response of the Rayleigh mode, as shown in Fig. 2(a). The two peaks in each time-domain response correspond to the arrivals of the first and the second acoustic wave packets. Fitting the delay time with the delay length, as shown in Fig. 2(b), yields a group velocity of  $v_g = 3,228 \text{ m/s}$ , which agrees well with the simulation.

We then calculate acoustic loss  $\gamma(L)$  for each device. This ratio reflects the accumulated acoustic propagation loss over a propagation distance of  $2L$ , as plotted in Fig. 2(c). By performing a linear fit to the measured loss as a function of the propagation length, we extract a Rayleigh-mode propagation

loss of 6.97 dB/mm at a central frequency of 1.84 GHz.

With the above measurement scheme, we study the frequency dependence of the acoustic loss. In dielectric crystals, a key intrinsic loss mechanism is due to interaction with thermal phonons in the medium<sup>31</sup>. In the case  $\omega\tau \ll 1$ , where  $\omega$  is the phonon angular frequency and  $\tau$  is the thermal phonon relaxation rate, the acoustic loss is described by the Akhiezer damping model:  $\alpha \propto T\omega^2$ , where  $\alpha$  is the propagation loss in dB/mm. When  $T$  decreases, or  $\omega$  increases such that  $\omega\tau \gg 1$ , it is in the Landau and Rumer regime<sup>32</sup>, such that  $\alpha \propto T\omega$ . In bulk single-domain LN, the Akhiezer loss with frequency dependence  $\alpha \propto \omega^2$  has been measured at room temperature over a broad frequency range extending to tens of gigahertz<sup>33,34</sup>.

To obtain the frequency dependence of acoustic loss, we repeated measurements of the Rayleigh mode at different frequencies on LNOI. As shown in Fig. 2(d), the propagation loss reduces quadratically as frequency decreases from 2.96 GHz to 0.73 GHz, with a fitting function of  $\alpha_{LNOI,f} = 1.294f^2 + 3.71$  in the unit of dB/mm, where  $f$  is the acoustic frequency in gigahertz. The frequency-dependent term of  $1.294f^2$  is consistent with the result measured in crystalline LN, while the frequency-independent residue loss of 3.71 dB/mm indicates that an extra loss channel exists on the LNOI platform.

In addition to frequency dependence, Akhiezer damping is theoretically expected to vary linearly with temperature. In contrast, acoustic loss due to defect scattering can exhibit a strong non-monotonic temperature dependence<sup>35</sup>. Defect scattering loss in amorphous materials is attributed to scattering by defect modes with a broad spectral distribution and can be well modeled with the tunneling model<sup>36</sup>. The ratio of the phonon wavelength  $\lambda$  to the phonon mean free path  $l$

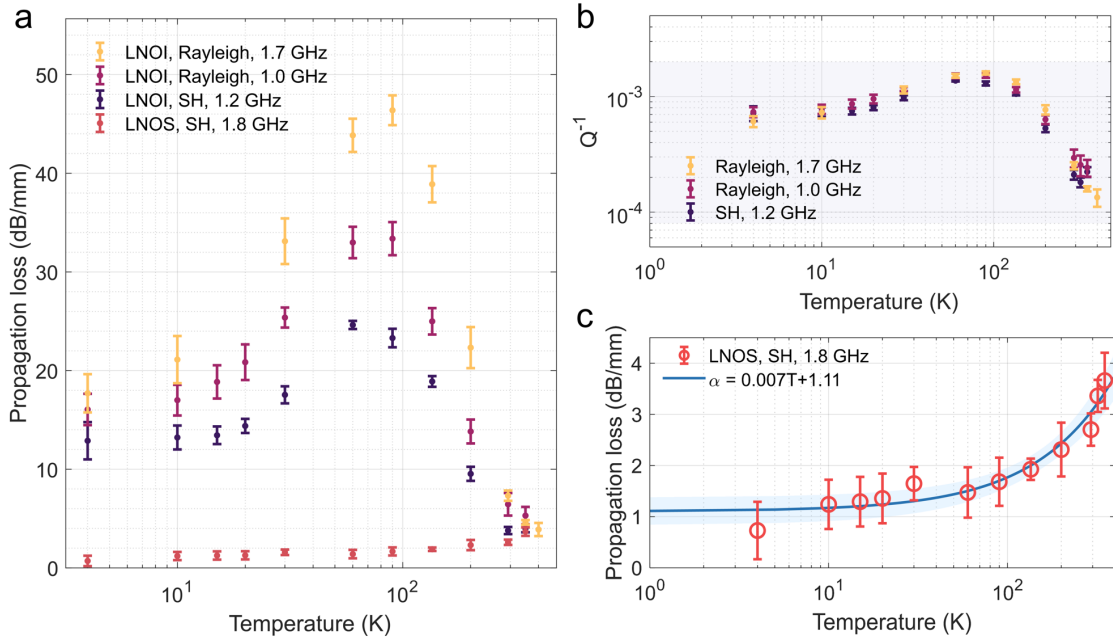


FIG. 3. **Temperature dependence of acoustic loss in TFLN platforms.** (a) Acoustic propagation loss of different acoustic modes measured in LNOI and LNOS in the temperature range from 4 to 400 K. (b) The inverse quality factors extracted from measurements on the LNOI sample. (c) Zoom-in view of the acoustic propagation loss versus temperature in LNOS with a linear fit, where  $T$  is the temperature (K).

of these studied amorphous materials<sup>35</sup> falls in the range of  $10^{-3} - 10^{-2}$ .

Motivated by these distinct temperature-dependent loss behaviors, we investigated the temperature-dependent acoustic loss of all four platforms. Because the intrinsic mechanical properties of LN are only weakly dependent on temperature<sup>37</sup>, temperature-dependent measurements are effective to infer the dominant acoustic loss channels in each platform.

Fig. 3(a) shows the temperature dependence of acoustic loss in LNOI and LNOS measured from 4 K to 400 K. In LNOS, the acoustic loss decreases with decreasing temperature; a zoom-in view of the data together with a linear fit is shown in Fig. 3(c), suggesting that the dominant loss mechanism could be Akhiezer damping. In contrast, the acoustic loss in LNOI exhibits a non-monotonic temperature dependence. For both Rayleigh and SH modes, the acoustic loss increases by 20–40 dB/mm as the temperature is lowered from room temperature to  $\sim 90$  K. As the temperature is further reduced, the acoustic loss decreases from its peak value but remains higher than the room temperature value.

We further calculate the inverse quality factor  $Q^{-1}$  for the LNOI sample using the measured propagation loss (in dB/mm) shown in Fig. 3(a). Here, the quality factor is defined as  $Q = 2\pi l/\lambda$ , with  $\lambda$  and  $l$  denoting the acoustic wavelength and phonon mean free path, respectively. The inverse quality factor is related to acoustic loss as  $\alpha = \frac{0.0546f}{Qv_g}$ , where  $f$  is the acoustic frequency and  $v_g$  is the group velocity. The extracted  $Q^{-1}$  is shown in Fig. 3(b) and exhibits a temperature dependence similar to that reported for amorphous  $\text{SiO}_2$  in a previous work<sup>35</sup>. The magnitude of  $Q^{-1}$  also falls within the characteristic range of glass<sup>35</sup>, suggesting that the buried-

oxide (BOX) layer in LNOI is a dominant loss channel for acoustic waves at low temperatures. Interestingly, as the temperature is increased from room temperature to 350–400 K, the acoustic loss reduces, supporting the interpretation that the frequency-independent residual loss originates from defect mode scattering in the BOX layer. At 400 K, the measured loss ( $4.56 \pm 0.33$  dB/mm) is consistent with the frequency-dependent term shown in Fig. 2(d) within experimental uncertainty, indicating that the loss contribution from the BOX layer becomes negligible at this temperature.

We also analyze the temperature-dependent acoustic propagation loss in bulk LN and suspended LN thin film. As shown in Fig. 4, the propagation losses measured on these two platforms show a linear temperature dependence from 4 K to room temperature, similar to LNOS. Attributing to the Akhiezer damping, the acoustic propagation loss extrapolated to different frequencies is of the same order of magnitude as previously reported values<sup>23,38</sup>. The linear fit indicates that bulk and suspended LN exhibit similar temperature-dependent acoustic loss but differ slightly in the temperature-independent residual loss. The latter could be attributed to defect scattering in crystals or at the released interface.

Compared with bulk LN, the acoustic propagation losses in TFLN platforms are higher by several dB/mm, even after excluding the loss associated with the BOX layer. To further investigate the origin of this excess loss, we examine the crystal quality and bonding interfaces of the TFLN platforms using scanning transmission electron microscopy (STEM). The STEM imaging was performed on an aberration-corrected Nion UltraSTEM electron microscope operated at 60 kV, using a semi-convergence angle of 32 mrad. High-angle an-

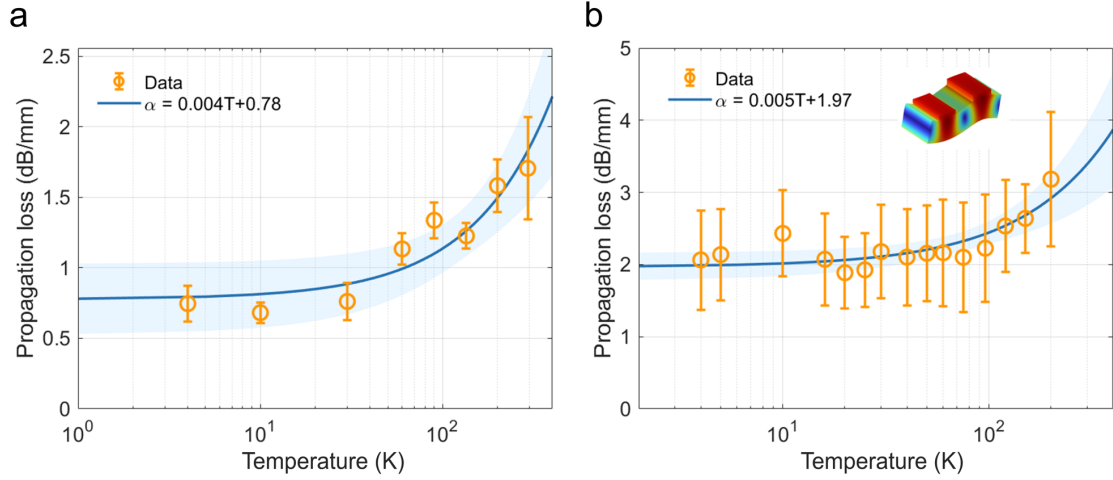


FIG. 4. Temperature-dependent acoustic propagation loss of (a). Fundamental Rayleigh mode of the bulk LN and (b). Fundamental asymmetric Lamb (A0) mode of the suspended LN. The inset shows the FEM simulation of the A0 mode profile of a 300 nm thick LN with 100 nm Au electrodes on top.

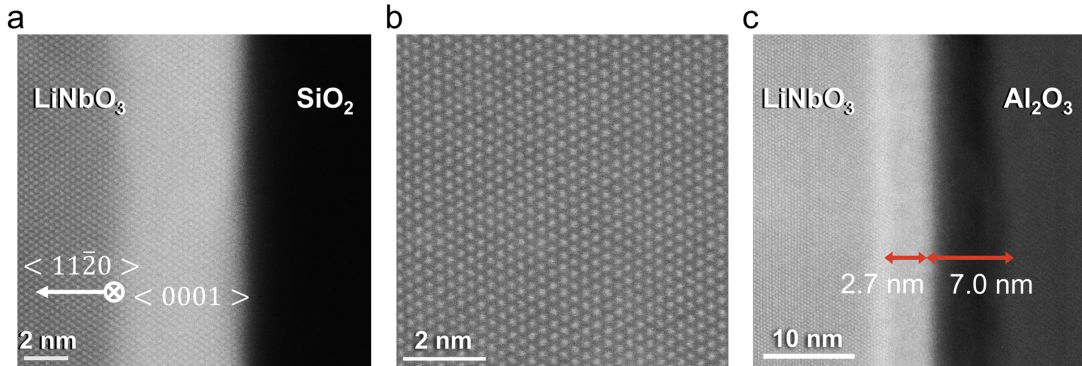


FIG. 5. Cross-sectional HAADF-STEM images of the TFLN sample along the  $<0001>$  zone axis, showing (a) Lattice continuity at the bonding interface of LNOI; (b) Atomic lattice periodicity of lithium niobate on LNOI; (c) Lattice continuity at the bonding interface of LNOS.

nular dark-field (HAADF) images were acquired with semi-collection angles ranging from 80-200 mrad, using a probe current of 10 pA. Fig. 5 (a), (b) shows STEM images of the bonding interface of the LNOI substrate, showing a good structural quality with a well-resolved LN lattice at the interface. An approximately 6 nm contrast variation is observed at the interface, which requires further analysis to determine its chemical composition. A similar bonding interface condition of LNOS is shown in Fig. 5 (c). Amorphization is observed at the interface, resulting in a brighter contrast of approximately 2.7 nm in the LN layer and a 7 nm-thick dark layer in the sapphire substrate. The darker contrast is likely due to ion milling during focused ion beam-transmission electron microscopy (FIB-TEM) sample preparation, which induces oxygen vacancies.

Although the transition layer at the bonding interface is only a few nanometers thick, crystal impurities in this region can introduce elastic disorder and defect-induced scattering, thereby providing a measurable loss channel for SAWs.

This mechanism may account for the observed temperature-independent propagation loss of approximately 1.97 dB/mm for the fundamental asymmetric Lamb (A0) mode in suspended LN and that of 1.11 dB/mm for the SH mode in LNOS. It may also contribute to the Rayleigh-mode loss in LNOI as part of the observed quadratic frequency-dependent loss.

In conclusion, we have systematically investigated acoustic attenuation mechanisms in thin-film lithium niobate (TFLN) platforms by comparing acoustic propagation loss across LNOI, LNOS, suspended LN thin films, and bulk LN over wide frequency and temperature ranges. We find that acoustic loss in LNOI exhibits a pronounced non-monotonic temperature dependence, which is characteristic of amorphous materials. The result suggests that the buried oxide layer is the dominant loss channel at low temperatures. At elevated temperatures, the loss associated with the buried oxide layer is suppressed, and the acoustic loss is governed primarily by Akhiezer damping in crystalline LN. In contrast, acoustic loss in LNOS, bulk LN, and suspended LN thin films is dominated

by Akhiezer damping over the entire measured temperature range and decreases monotonically with decreasing temperature. These results indicate that acoustic loss in LNOI can be mitigated by operating at elevated temperatures or by replacing the buried oxide layer with a crystalline substrate. In addition, high-resolution HAADF-STEM imaging reveals nanoscale interfacial disorder at the bonding interface, which may introduce an additional loss channel in TFLN devices relative to bulk LN. These results clarify the physical origins of acoustic loss in TFLN platforms and provide important material and structural guidelines for minimizing acoustic loss in future phononic, acousto-optic, piezo-optomechanics, and quantum acoustic devices.

## ACKNOWLEDGMENTS

This work is supported by the National Science Foundation (Award No. ITE-2134345 and OSI-2326746) and the DARPA MTO SOAR program (Award No. HR0011363032). Part of this work was conducted at the Washington Nanofabrication Facility and Molecular Analysis Facility, a National Nanotechnology Coordinated Infrastructure (NNCI) site at the University of Washington, with partial support from the National Science Foundation via award nos. NNCI-2025489. The electron microscopy part of this work was supported by the National Science Foundation (NSF) through a Materials Research Science and Engineering Center (DMR-2308979).

## DATA AVAILABILITY

The data that supports the findings of this study are available from the corresponding author upon reasonable request.

- <sup>1</sup>R. Lu and S. Gong, *Journal of Micromechanics and Microengineering* **31**, 114001 (2021).
- <sup>2</sup>X. Tong, Y. Zou, Z. Wen, Z. Liu, T. Luo, J. Zhou, H. Liu, Y. Ren, Q. Xu, W. Liu, *et al.*, *Microsystems & Nanoengineering* **10**, 130 (2024).
- <sup>3</sup>B. Li, Q. Lin, and M. Li, *Nature* **620**, 316 (2023).
- <sup>4</sup>K. Ye, H. Feng, R. Te Morsche, C. Wei, Y. Klaver, A. Mishra, Z. Zheng, A. Keloth, A. Tarik Işık, Z. Chen, *et al.*, *Science Advances* **11**, eadv4022 (2025).
- <sup>5</sup>G. Kurizki, P. Bertet, Y. Kubo, K. Mølmer, D. Petrosyan, P. Rabl, and J. Schmiedmayer, *Proceedings of the National Academy of Sciences* **112**, 3866 (2015).
- <sup>6</sup>K. J. Satzinger, Y. Zhong, H.-S. Chang, G. A. Peairs, A. Bienfait, M.-H. Chou, A. Cleland, C. R. Conner, É. Dumur, J. Grebel, *et al.*, *Nature* **563**, 661 (2018).
- <sup>7</sup>A. Bienfait, K. J. Satzinger, Y. Zhong, H.-S. Chang, M.-H. Chou, C. R. Conner, É. Dumur, J. Grebel, G. A. Peairs, R. G. Povey, *et al.*, *Science* **364**, 368 (2019).
- <sup>8</sup>H. Qiao, É. Dumur, G. Andersson, H. Yan, M.-H. Chou, J. Grebel, C. R. Conner, Y. J. Joshi, J. M. Miller, R. G. Povey, *et al.*, *Science* **380**, 1030 (2023).
- <sup>9</sup>A. Bozkurt, H. Zhao, C. Joshi, H. G. LeDuc, P. K. Day, and M. Mirhosseini, *Nature Physics* **19**, 1326 (2023).
- <sup>10</sup>K. Länge, B. E. Rapp, and M. Rapp, *Analytical and bioanalytical chemistry* **391**, 1509 (2008).
- <sup>11</sup>M. Aspelmeyer, T. J. Kippenberg, and F. Marquardt, *Reviews of Modern Physics* **86**, 1391 (2014).
- <sup>12</sup>D. A. Golter, T. Oo, M. Amezcu, I. Lekavicius, K. A. Stewart, and H. Wang, *Physical Review X* **6**, 041060 (2016).
- <sup>13</sup>S. Maity, L. Shao, S. Bogdanović, S. Meesala, Y.-I. Sohn, N. Sinclair, B. Pingault, M. Chalupnik, C. Chia, L. Zheng, *et al.*, *Nature communications* **11**, 193 (2020).
- <sup>14</sup>R. Sasaki, Y. Nii, and Y. Onose, *Nature communications* **12**, 2599 (2021).
- <sup>15</sup>R. Peng, A. Ripin, Y. Ye, J. Zhu, C. Wu, S. Lee, H. Li, T. Taniguchi, K. Watanabe, T. Cao, *et al.*, *Nature Communications* **13**, 1334 (2022).
- <sup>16</sup>M. Chen, J. C. Owens, H. Puterman, M. Schäfer, and O. Painter, *Science Advances* **10**, eado6240 (2024).
- <sup>17</sup>S.-J. Tang, M. Zhang, J. Sun, J.-W. Meng, X. Xiong, Q. Gong, D. Jin, Q.-F. Yang, and Y.-F. Xiao, *Nature Photonics* **17**, 951 (2023).
- <sup>18</sup>Q. Liu, H. Li, and M. Li, *Optica* **6**, 778 (2019).
- <sup>19</sup>Q. Lin, S. Fang, Y. Yu, Z. Xi, L. Shao, B. Li, and M. Li, *Nature Communications* **16**, 4501 (2025).
- <sup>20</sup>S. P. Selvin, M. Esfandyarpour, A. Ji, Y. J. Lee, C. Yule, J.-H. Song, M. Taghinejad, and M. L. Brongersma, *Science* **389**, 516 (2025).
- <sup>21</sup>W. Jiang, C. J. Sarabalis, Y. D. Dahmani, R. N. Patel, F. M. Mayor, T. P. McKenna, R. Van Laer, and A. H. Safavi-Naeini, *Nature communications* **11**, 1166 (2020).
- <sup>22</sup>S. Barzanjeh, A. Xuereb, S. Gröblacher, M. Paternostro, C. A. Regal, and E. M. Weig, *Nature Physics* **18**, 15 (2022).
- <sup>23</sup>A. Slobodnik Jr, P. Carr, and A. Budreau, *Journal of Applied Physics* **41**, 4380 (1970).
- <sup>24</sup>L. Shao, D. Zhu, M. Colangelo, D. Lee, N. Sinclair, Y. Hu, P. T. Rakich, K. Lai, K. K. Berggren, and M. Lončar, *Nature Electronics* **5**, 348 (2022).
- <sup>25</sup>M. Shen, J. Xie, C.-L. Zou, Y. Xu, W. Fu, and H. X. Tang, *Applied Physics Letters* **117** (2020).
- <sup>26</sup>R. Lu, Y. Yang, A. E. Hassanien, and S. Gong, *IEEE Transactions on Microwave Theory and Techniques* **69**, 3246 (2021).
- <sup>27</sup>T. Luschmann, A. Jung, S. Geprägs, F. X. Haslbeck, A. Marx, S. Filipp, S. Gröblacher, R. Gross, and H. Huebl, *Materials for Quantum Technology* **3**, 021001 (2023).
- <sup>28</sup>S. V. Biryukov, Y. V. Gulyaev, V. V. Krylov, and V. P. Plessky, *Surface acoustic waves in inhomogeneous media*, Vol. 20 (Springer, 1995).
- <sup>29</sup>R. Manenti, M. Peterer, A. Nersisyan, E. Magnusson, A. Patterson, and P. Leek, *Physical Review B* **93**, 041411 (2016).
- <sup>30</sup>E. A. Wollack, A. Y. Cleland, P. Arrangoiz-Arriola, T. P. McKenna, R. G. Gruenke, R. N. Patel, W. Jiang, C. J. Sarabalis, and A. H. Safavi-Naeini, *Applied Physics Letters* **118** (2021).
- <sup>31</sup>T. Woodruff and H. Ehrenreich, *Physical Review* **123**, 1553 (1961).
- <sup>32</sup>M. Pomerantz, *Proceedings of the IEEE* **53**, 1438 (2005).
- <sup>33</sup>I. Bajak, A. McNab, J. Richter, and C. Wilkinson, *The Journal of the Acoustical Society of America* **69**, 689 (1981).
- <sup>34</sup>C. Wen and R. Mayo, *Applied Physics Letters* **9**, 135 (1966).
- <sup>35</sup>R. O. Pohl, X. Liu, and E. Thompson, *Reviews of Modern Physics* **74**, 991 (2002).
- <sup>36</sup>W. A. Phillips, *Journal of low temperature physics* **7**, 351 (1972).
- <sup>37</sup>R. Smith and F. Welsh, *Journal of applied physics* **42**, 2219 (1971).
- <sup>38</sup>R. Lu, Y. Yang, S. Link, and S. Gong, *IEEE Transactions on Microwave Theory and Techniques* **69**, 541 (2020).